Supporting Information for

Topological defects in hexagonal manganites - Inner structure and emergent electrostatics.

M. E. Holtz, K. Shapovalov, J. A. Mundy, C. S. Chang, Z. Yan, E. Bourret, D. A. Muller, D. Meier, A. Cano

Note 1 STEM data acquisition and processing

$ErMnO_3$ platelets were oriented by Laue diffraction such that the specimen would be imaged down the $[1\bar{1}0]$ zone axis of the crystal in TEM. Cross-sectional TEM samples were prepared using an FEI Strata 400 Focused Ion Beam with a final milling step of 2 keV to minimize surface damage. The TEM specimens were imaged on a 100 keV Nion UltraSTEM optimized for EELS imaging (30 mrad convergence angle, 80-130 pA of usable beam current, ~ 1 Å spatial resolution).

The Er distortions – and from that, the local phase, amplitude and polarization – were quantified from high-angle annular dark field (HAADF) STEM images. To precisely measure erbium displacements which are on the order of tens of picometers, high quality STEM images are prepared by cross-correlating several (~ 20) fast images to reduce scan noise. The images were calibrated by measuring the peaks in the Fourier transform. The images are then background subtracted using morphological opening operations and Wiener Filtered using the thickness obtained from electron energy-loss spectroscopy. The rough atomic positions of the erbium atoms were then determined by segmentation using a grey threshold followed by the watershed algorithm, followed by 2-D Gaussian fitting to refine the positions. The displacement of each atom was compared to its neighboring atoms in the atomic plane. The phase and amplitude of the distortion was calculated by comparing the displacements of the three atoms and fitting to eq 1 of the main text, as illustrated in Figure 1a.

In Figure S1 and Figure S2, we show the data from domain walls and vortices, respectively. These figures include the background subtracted and Wiener filtered data (first row), the data with the Er displacement color overlay, which monotonically tracks the polarization, (second row), the phase Φ (third row – for Figure S1 this is modulo $2\pi/3$), and the amplitude Q (last row). From these images one can see one-to-one correspondence between $\uparrow\uparrow\downarrow$ pattern and the positive average displacement of erbium ions, which

we attribute to the polar Γ_2^- mode and thus to the positive polarization. Similarly, one can see one-to-one correspondence between $\downarrow\downarrow\uparrow$ pattern and negative polarization.

Figure S3 shows more details on the data processing behind Figure 2 in the main text. Figure S3a shows the data processing for all of the walls in Zr-doped $ErMnO_3$. The raw data including data from 90 images is shown by black dots, which is binned down into blue circles for viewing purposes (the binned data is plotted in Figure 2e,f). The raw data is fit (red line) with 95% prediction intervals (magenta lines). Because the domain walls meander in the specimens, we include a range of angles in our analysis for charged and neutral walls, called the acceptance angle. Figure S3b shows how ξ_6 changes as the acceptance angle is changed from 1 to 10 degrees, the results do not change within error except the Zr-doping charged walls appear to become broader. To get meaningful statistics without introducing error from including domain walls of varying inclination, we use an acceptance angle of 5 degrees.

We note that we do not observe large broadening of the domain walls due to overlap of two domains in projection – as would occur if the domain wall was at an angle with respect to the electron beam or if there were jogs in the domain wall in projection. This overlap was observed in Ref. 17. In their data, the overlap of two domains in projection is clearly visible as a reduction in contrast on a specific atomic position as well as smearing of the atomic column. The overlapping domain wall effect is not observed in our thinner samples and which is fundamentally different from the atomic displacements addressed in our work (see Figure S5). While we do observe domain wall overlap in thicker regions of the specimen, as seen in Figure S5d, this is not generally observed in our thinner regions (20-50 nm). From our statistics, we exclude images which are taken in thicker regions of the specimen that may show an overlap of two domains in projection.

Note 2 STEM observations of vortex in undoped $ErMnO_3$

In Figure S4 we show HAADF-STEM data from a trimerization vortex in undoped $ErMnO_3$ sample along with $\Phi(\theta)$ and $Q(r)$ evolutions, similar to the data presented on $Er_{1-x}Zr_xMnO_3$ in Figure 3 of the main text. Six domains with different Φ_n's merge at the central point of the vortex, which is seen in the color-overlaid phase map in Figure S4a. The corresponding amplitude is shown in Figure S4c. In Figure S4b, we plot the trimerization phase Φ as a function of the angle θ around the central point for different distances from this point. Φ has a step-like nature for distances $\gtrsim 3$ nm where it corresponds to a discrete set of trimerization domains separated by domain walls, except in regions where the domain width is on the same order as ξ_6, such as in the $\Phi = \pi/3$, $2\pi/3$ regions shown in yellow and green in part (a). In Figure S4d, the trimerization amplitude Q drops to

zero at the vortex central point, while it recovers its bulk value within a distance of ~ 18 Å in $ErMnO_3$.

Note 3 Justification of the constant-amplitude approximation for eq 4

In order to show that the constant-amplitude approximation is a reasonable approximation that allows a straightforward and accurate extraction of ξ_6 from STEM in our system, we compare the exact $\Phi(x)$ profile obtained by minimizing eq 2 using numerical methods. This comparison shows that the deviation of our analytical result (eq 4) from the numerical one is negligible.

We minimize the Landau energy F (eq 2) by solving the system of the corresponding Euler-Lagrange equations

$$\partial F/\partial Q = \vec{\nabla} \cdot \partial F/\partial(\nabla Q),$$
$$\partial F/\partial \Phi = \vec{\nabla} \cdot \partial F/\partial(\nabla \Phi)$$

numerically for the 1D geometry of a domain wall, without using any approximations. For this, we use COMSOL Multiphysics, with the numerical values of the material constants corresponding to ξ and ξ_6 extracted from the STEM images (Figures 2, 3).

The numerically obtained $\Phi(x)$, compared with the analytical one given by eq 4, is shown in Figure S6. The values of ξ_6 that correspond to these two solutions differ by 6%, the numerical one being slightly wider, which can be linked to the coupling of $\Phi(x)$ to the non-constant $Q(x)$ inside the wall. Thus the extraction of ξ_6 by fitting STEM $\Phi(x)$ profile with eq 4 is associated with a negligibly small error, from which we conclude that the use of the constant-amplitude approach is justified a-posteriori.

Note 4 Analytical description of trimerization amplitude at the wall

We begin with the Euler-Lagrange equation for the trimerization amplitude $\partial F/\partial Q = \vec{\nabla} \cdot \partial F/\partial(\nabla Q)$ obtained after the substitution of the distribution of phase (eq 4) into eq 2:

$$\frac{a}{g}Q + \frac{b}{g}Q^3 + \frac{c+c'}{g}Q^5 + \left(\frac{Q}{9\xi_6^2} - \frac{c'Q^5}{g}\right)\frac{1}{\cosh^2(x/\xi_6)} = \frac{d^2Q}{dx^2}. \tag{S1}$$

In the following, we neglect the influence of the high-order term $\frac{c+c'}{g}Q^5$ in eq S1.

Since the change of $Q(x)$ inside the wall is small compared to its bulk value $[Q(x) = Q_0(1+q(x)),\ |q(x)| \ll 1]$, eq S1 can be then linearized into

$$\frac{2q}{\xi^2} + \frac{4}{9\xi_6^2}\frac{1}{\cosh^2(x/\xi_6)} = \frac{d^2q}{dx^2}. \tag{S2}$$

One can see that eq S2 is controlled by two independent scales: $\xi \simeq \sqrt{g/|a|}$ and $\xi_6 \simeq \sqrt{g/(3|c'|Q_0^4)} \simeq \xi\sqrt{-b^2/(3a|c'|)}$; therefore, the width of the domain wall in terms of trimerization amplitude is defined by the interplay between these two scales. The solution to eq S2 can be obtained analytically in the reciprocate space, with Fourier transform introduced as $F[q(x)](k) \equiv \widetilde{q}(k) = (1/\sqrt{2\pi})\int_{-\infty}^{\infty} q(x)\exp(-ikx)dx$. It reads:

$$\widetilde{q}(k) = -\frac{2\xi^2}{9\xi_6^2}\frac{1}{1+\xi^2k^2/2}F\left[\frac{1}{\cosh^2(x/\xi_6)}\right](k), \tag{S3}$$

leading to the following distribution of the trimerization amplitude $Q(x)$ in the wall:

$$Q(x) = Q_0 - Q_0\frac{\sqrt{2}}{9}\frac{\xi}{\xi_6^2}\left(\exp\left(-\frac{\sqrt{2}}{\xi}|x|\right) * \frac{1}{\cosh^2(x/\xi_6)}\right), \tag{S4}$$

where $(f(x) * g(x)) = \int_{-\infty}^{\infty} f(t)g(x-t)dt$ designates the convolution operation. Note that the two convoluted functions in eq S4 have independent widths controlled by the two correlation lengths in the system: $\exp(-\sqrt{2}|x|/\xi)$ has width $\sim \xi$, while the function $1/\cosh^2(x/\xi_6)$ has width $\sim \xi_6$. In the following, we estimate the width of the convolution in two distinct regimes.

Close to the temperature of trimerization transition, when $\xi_6 \gg \xi$, eq S4 rewrites into

$$Q(x) = Q_0\left(1 - \frac{2}{9}\frac{\xi^2}{\xi_6^2}\frac{1}{\cosh^2(x/\xi_6)}\right). \tag{S5}$$

Thus, near the transition point, the correlation length ξ_6 controls all the domain-wall-related effects.

For the case $\xi \sim \xi_6$, one can estimate the width of the profile $Q(x)$ by referring, for example, to the convolution of two Gaussian functions:

$$\left(\exp\left(-\frac{x^2}{\sigma_1^2}\right) * \exp\left(-\frac{x^2}{\sigma_2^2}\right)\right) = \sqrt{\pi}\frac{\sigma_1\sigma_2}{\sqrt{\sigma_1^2+\sigma_2^2}}\exp\left(-\frac{x^2}{\sigma_1^2+\sigma_2^2}\right), \tag{S6}$$

in line with which eq S4 can be approximated as

$$Q(x) \approx Q_0\left(1 - \frac{1}{\kappa}\frac{\xi^2}{\xi_6\widetilde{\xi_6}}\frac{1}{\cosh^2(x/\widetilde{\xi_6})}\right), \tag{S7}$$

where $\kappa = 9/\sqrt{2\pi}$ and $\widetilde{\xi_6} = \xi_6\sqrt{1+\xi^2/\xi_6^2}$ is the length scale controlling the $Q(x)$ profile. One can see that for $\xi \sim \xi_6$ the wall width in terms of the trimerization amplitude Q ($\sim \sqrt{\xi^2+\xi_6^2}$) will always exceed the width of the same wall in terms of the phase Φ ($\sim \xi_6$).

Note that in the case $\xi_6 \gg \xi$ eq S7 rewrites with good precision into eq S5 with slightly different value for κ: $\kappa = 9/2$ for $\xi_6 \gg \xi$. From this, we conclude that there is a dependence of κ on the ratio ξ_6/ξ, though it is weak for the regime of physical interest $\xi_6/\xi \gtrsim 1$.

Note 5 Analytical description of trimerization order parameter in the vortex

For the analytical description of vortices, we consider an ideal vortex in which the six domains are equally represented. To reproduce this case, we can assume $\Phi \approx \Phi(\theta)$ and $Q \approx Q(r)$ in the Euler-Lagrange equation for the phase to get:

$$\left(\frac{Q(r)}{Q_0}\right)^2 \sin^2 6\Phi = \frac{1}{(r/\xi_6)^2}\frac{\partial^2 6\Phi}{\partial\theta^2}. \tag{S8}$$

If $\xi_6 \gtrsim \xi$ the amplitude can be further approximated as $Q(r) \approx Q_0$, which renders the equation equivalent to eq 3 with $x = r\theta$. The validity of this approximation can be checked *a-posteriori*. Thus, we can make use of the family of solutions to eq S8

$$\Phi(r,\theta) = \frac{\pi}{6} + \frac{1}{3}\mathrm{am}\left(\frac{r\theta}{k\xi_6}\middle|k^2\right), \tag{S9}$$

where $\mathrm{am}(F|k^2)$ is the Jacobi amplitude, further imposing the condition of periodicity $\Phi(\theta+2\pi) = \Phi(\theta) + 2\pi$. This restricts the k parameter to that satisfying $2kF(\pi/2|k^2) = \pi r/(3\xi_6)$, where $F(\psi|k^2) = \int_0^\psi dt/\sqrt{1-k^2\sin^2(t)}$ is the elliptic integral of the first kind. With this, the resulting distribution $\Phi(x,y)$ following from eq S9 is shown in Figure S7. This solution has two distinct regimes, defined by the distance from the central point of the vortex. Far enough from the vortex central point, where the distance between the walls is larger than their effective width ($\frac{2\pi r}{6} \gtrsim 4\xi_6$), eq S9 represents six individual domain walls of thicknesses $\sim 4\xi_6$ placed at 60° from each other. On the other hand, the overlap of the domain walls near the vortex central point ($r \lesssim 4\xi_6$) results in another regime in which the distribution of the trimerization phase is $\Phi(\theta) \approx \theta$. This analysis confirms that the central point of the vortex is in fact a singular point in which $|\nabla\Phi(\theta)| \approx 1/r$ diverges.

To track main features of the distribution of the amplitude Q near this singularity, we

consider the corresponding Euler-Lagrange equation with $\Phi(\theta) = \theta$:

$$aQ(r) + bQ^3(r) + (c + c')Q^5(r) = \frac{g}{r}\left(Q'(r) - \frac{Q(r)}{r}\right) + gQ''(r). \tag{S10}$$

In the immediate vicinity of the singularity the dominant term is $\frac{g}{r}\left(Q'(r) - \frac{Q(r)}{r}\right)$, which drives to a linear drop of Q to zero: $Q(r) \simeq \frac{r/\xi}{\sqrt{2 + (r/\xi)^2}} Q_0 \underset{r\to 0}{\approx} \frac{r}{\sqrt{2}\xi} Q_0$. Besides, one can see that the characteristic length of change of Q is ξ.

Note 6 Numerical description of trimerization order parameter in the vortex

For numerical simulation of the vortex, we solve the set of Euler-Lagrange equations corresponding to the minimal free energy (eq 2 of the main text) using the method of finite elements implemented in the software COMSOL Multiphysics.

In order to model the core of the vortex (where $|\nabla\Phi| \to \infty$), we cut a small circular region of radius r_1=0.4 Å around the singular point and apply the following boundary condition at the circular boundary:

$$\Phi\big|_{r=r_1} = \theta - \theta_0, \qquad Q\big|_{r=r_1} = 0,$$

where θ_0 is the constant fixing the rotational degree of freedom of the vortex. At the outer boundary of the zone of calculation ∂D, the boundary conditions correspond to the set of six domain walls:

$$\Phi\big|_{\partial D} = -3\pi + \frac{2}{3}\sum_{i=1}^{6} \arctan\left[\exp\left(\frac{r(\theta - \theta_i)}{\xi_6}\right)\right], \qquad \frac{\partial D}{\partial r}\bigg|_{\partial D} = 0.$$

Here constants θ_i are fixing the angular positions of the six domain walls at the outer boundary. The constant θ_0 describing the rotational degree of freedom of the vortex is thus linked to them as $\theta_0 = \sum_{i=1}^{6} \theta_i/6$.

The triangular mesh is used for the finite-elements calculation, with mesh size varying from 0.04 Å around the vortex core to 0.2 Å at the domain wall to 20 Å at the bulk. For the case of the non-symmetric vortex, we observe a non-negligible influence of the radius of the circular cut-off region on the distribution of $\mathbf{Q}(\mathbf{r})$ around the vortex core, which we relate to the asymmetry of the core. In order to minimize this influence and give a reasonable estimate to the distribution of the order parameter in such a vortex,

we perform a non-self-consistent solution in two steps. For the first step, we seek the distribution $\Phi(\mathbf{r})$ for the fixed $Q(r) = Q_0 \dfrac{r/\xi}{\sqrt{2+(r/\xi)^2}}$. As the second step, we fix the obtained $\Phi(\mathbf{r})$ distribution and refine $Q(\mathbf{r})$ accordingly.

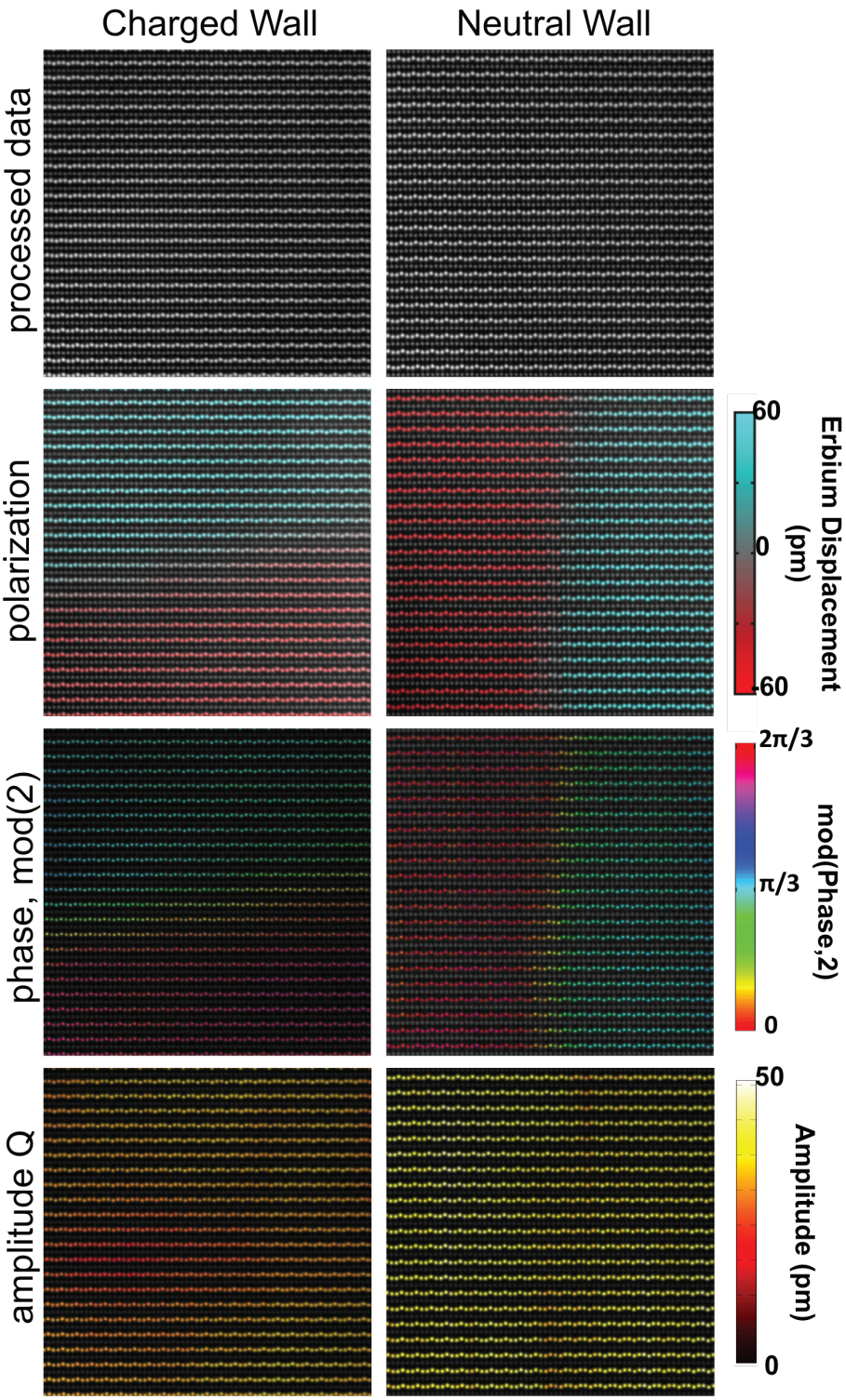

Figure S1. Domain walls in undoped $ErMnO_3$. A charged domain wall is on the left and a neutral domain wall is on the right. Top row, background subtracted and Wiener Filtered data. 2nd row, Color overlay indicating the Er displacements, and thus the polarization, of the image in the top row. Turquoise signifies polarization up and red polarization down, according to the color bar. 3rd row, The phase, modulo $2\pi/3$, across the domain wall. A continuous shift is seen from red to turquoise. Last row, the Amplitude Q. Field of view is 12.2 nm.

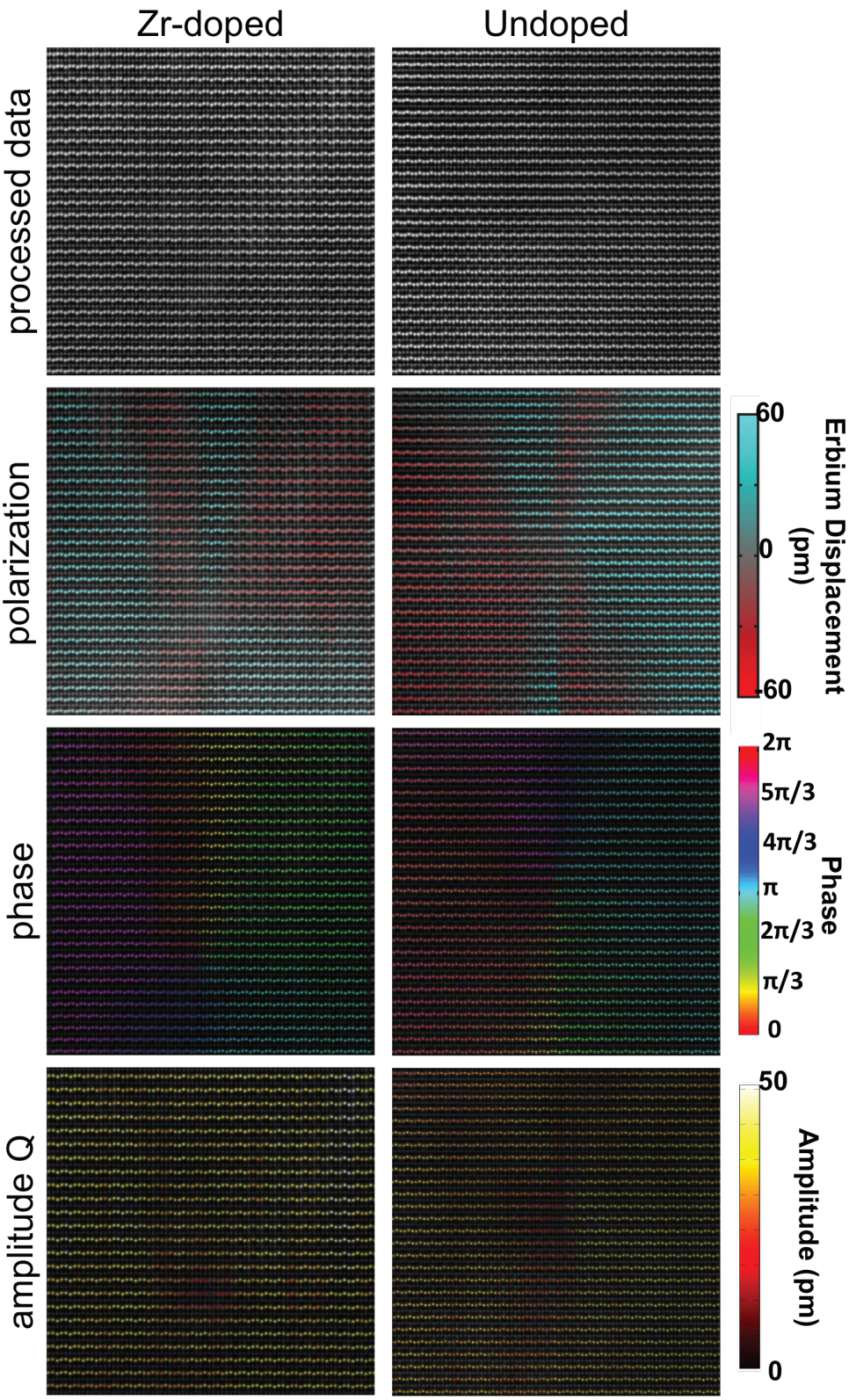

Figure S2. Vortices in Zr-doped and undoped $ErMnO_3$. Zr-doped is on the left and undoped $ErMnO_3$ is on the right. Top row, background subtracted and Wiener Filtered data. 2nd row, Color overlay indicating the Er displacements, and thus the polarization, of the image in the top row. Turquoise signifies polarization up and red polarization down, according to the color bar. 3rd row, The phase map, showing the 6 domains comprising the vortices. Last row, the Amplitude Q. Field of view is 15 nm.

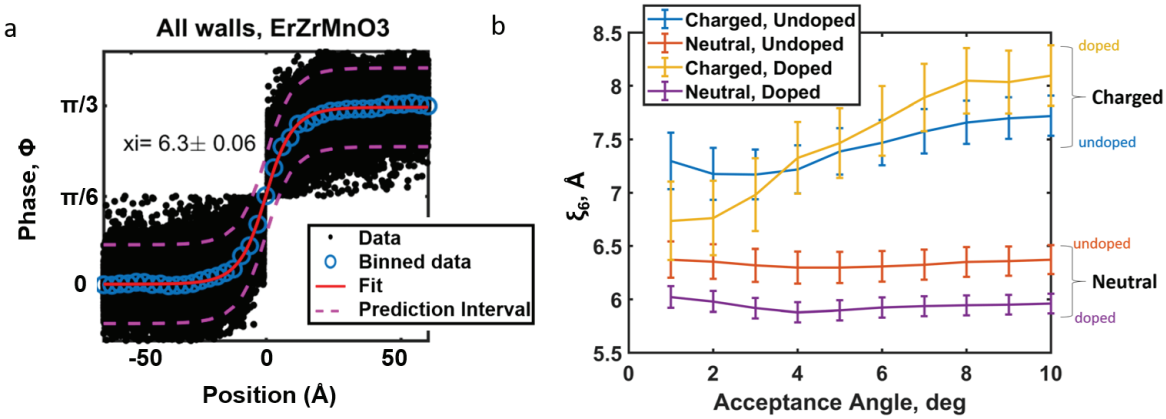

Figure S3. (a) Phase as a function of position across the domain wall, with black dots representing the individual observations on atomic columns and the blue circles representing the binned data. The red line is the fit to the dots. The 95% prediction interval is shown for the fit. (b) How ξ_6 changes as we include domains with angles that fall within $\pm\alpha$ degrees of the domain wall, where α is the acceptance angle.

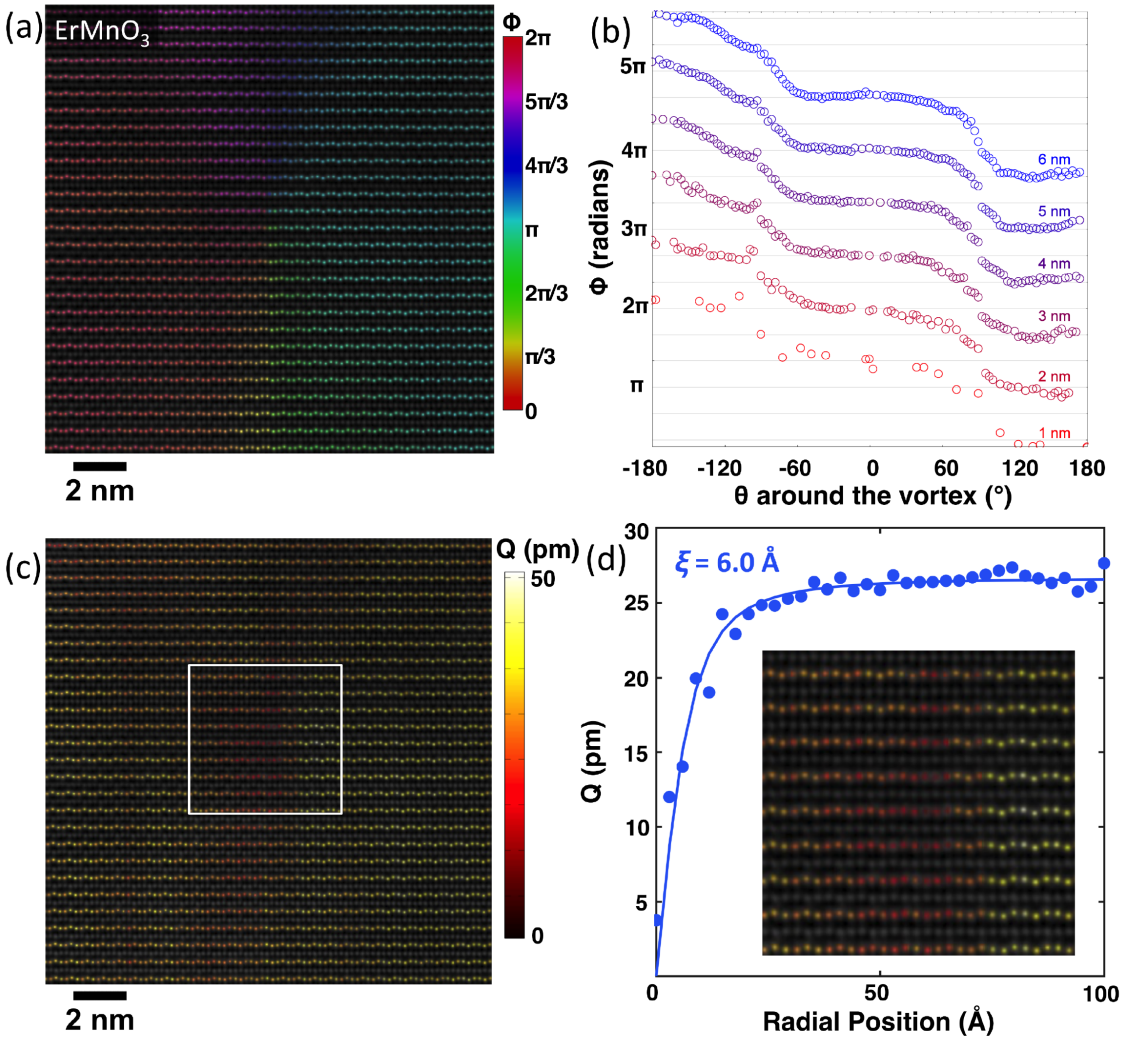

Figure S4. Atomic vortex structure in undoped $ErMnO_3$. (a) HAADF-STEM overlay of the phase of the vortex, showing a clockwise progression of phase from 0 to 2π. (b) Amplitude of the distortions, showing a decrease of Q at the vortex core. (c) Evolution of the phase wrapping around the vortex core at different radii. Solid points represent experimental measurement and lines show simulated results. (d) Plot of the amplitude with radial distance from the vortex core.

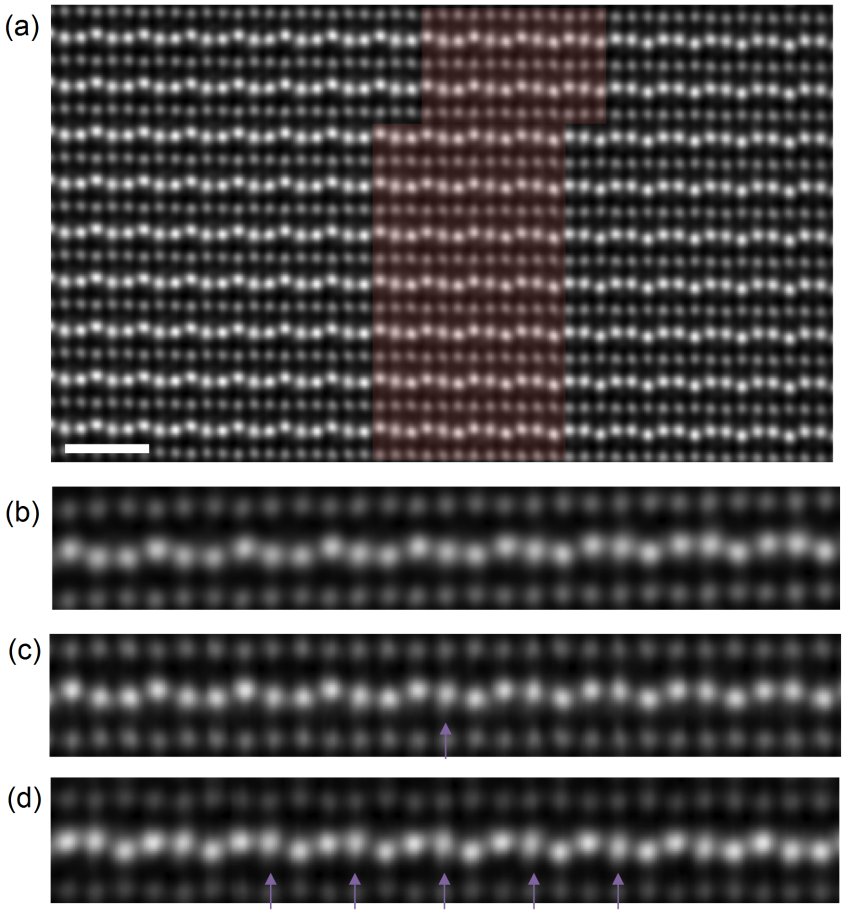

Figure S5. (a) HAADF-STEM image of a neutral domain wall, with a 1 nm scale bar. The unit cells around the domain wall are highlighted. (b) Zoomed-in region showing the progression of the atomic columns across a domain wall in a thin region. In comparison to reference 17, there is not a decrease in atomic contrast or a smearing of atomic positions, indicating there are not regions of the image that have two overlapping domains in projection. (c) Slightly thicker region where we see minimal smearing if any. (d) The thickest region, where we see two domains overlapping in projection, where the atomic column intensity is lower due to electron beam channelling on the two atomic columns (pointed out by the arrows).

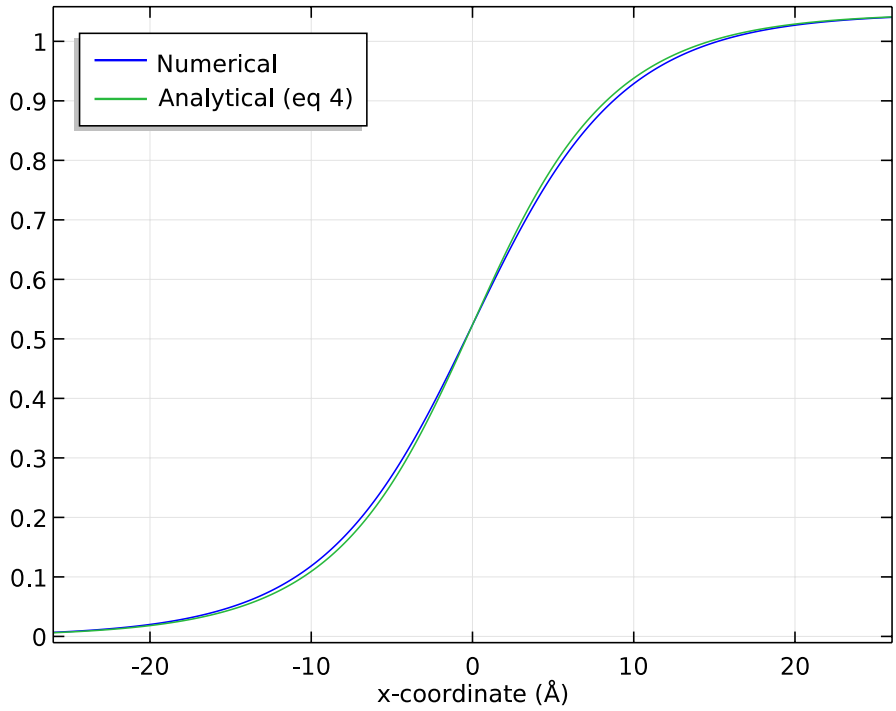

Figure S6. Comparison of distributions $\Phi(x)$ obtained using two different methods: numerical result obtained directly from eq 2, and analytical result (eq 4) obtained in the approximation of the constant amplitude (blue and green lines, respectively). The difference between the values of ξ_6 extracted using these two methods is 6%.

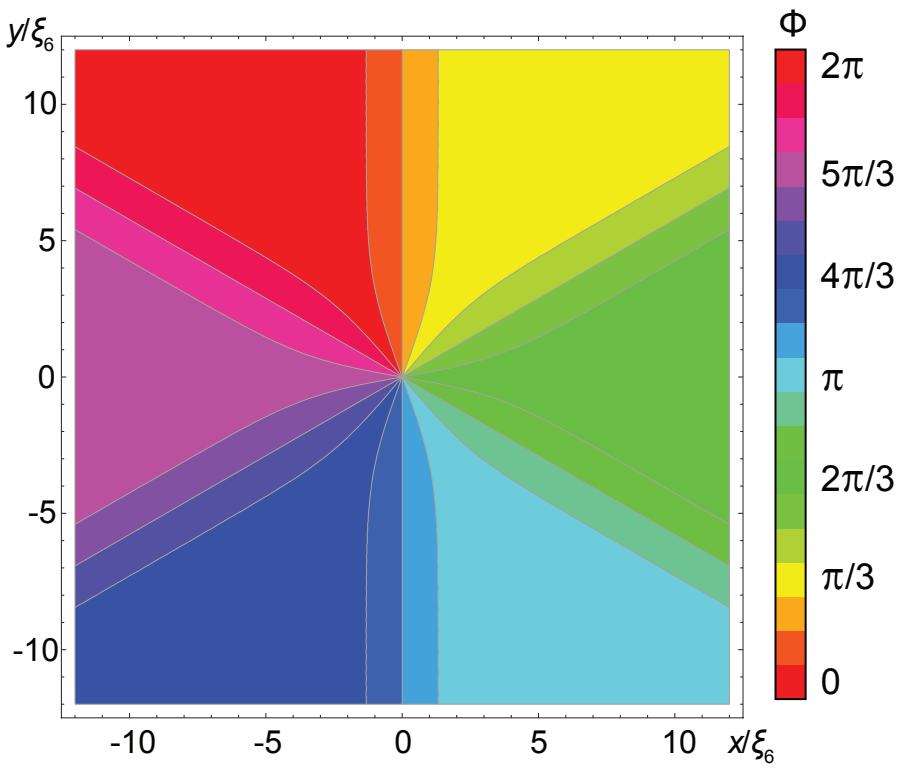

Figure S7. Contour plot for the evolution of phase around the vortex given by analytical expression for phase. The distribution according to eq S9 is shown, with imposed condition of periodicity $\Phi(\theta + 2\pi) = \Phi(\theta) + 2\pi$. This evolution of phase reproduces all features of vortex observed in the framework of self-consistent numerical calculations (Figure 4 of the main text).